ADVANCED MATERIALS

Supporting Information

for *Adv. Mater.,* DOI: 10.1002/adma.202105120

A Tissue-Like Soft All-Hydrogel Battery

*Tingting Ye, Jiacheng Wang, Yiding Jiao, Luhe Li, Er He, Lie Wang, Yiran Li, Yanjing Yun, Dan Li, Jiang Lu, Hao Chen, Qianming Li, Fangyan Li, Rui Gao, Huisheng Peng, and Ye Zhang**

Supporting Information

A tissue-like soft all-hydrogel battery

*Tingting Ye, Jiacheng Wang, Yiding Jiao, Luhe Li, Er He, Lie Wang, Yiran Li, Yanjing Yun, Dan Li, Jiang Lu, Hao Chen, Qianming Li, Fangyan Li, Rui Gao, Huisheng Peng, Ye Zhang**

Materials. Acrylic amide (AAM, 99.0%), lithium chloride (LiCl, 99.0%), methylene-bis-acrylamide (MBA, 99.0%) and rhodamine B were purchased from Shanghai Aladdin Biochemical Technology Co. Ltd. Ammonium persulphate (APS, 98%) was purchased from Nanjing Chemical Reagent Co. Ltd. N,N,N',N'-tetramethylethylenediamine (TEMED, 99.0%) was purchased from Alfa Aesar. $LiMn_2O_4$ (LMO) was purchased from Shanghai Aidu Chemical Technology Co. Ltd., and $LiTi_2(PO_4)_3$ (LTP) was purchased from Jiangxi KingLi Technology Co. Ltd. Carbon nanotube (CNT) dispersion (TNWDMC-MC8) was purchased from Chengdu Organic Chemicals Co. Ltd. Polyvinylidene fluoride (PVDF), active carbon (AC), and super P were purchased from Hefei Kejing Material Technology Co. Ltd. N-methyl-pyrrolidone (NMP, 99.0%) and zinc trifluoromethanesulfonate ($Zn(OTf)_2$, 98%) were purchased from Shanghai Macklin Biochemical Co. Ltd. All chemicals were used as received.

Fabrication of self-healing all-hydrogel battery. Polyacrylamide (PAM)/agar/CNT self-healing conductive hydrogel was prepared as follows. 1 M AAm and 0.05 M agar were added into 30 wt% CNT/water dispersion and stirred for 1 hour at 90 ℃. Afterward, 0.28 wt% (relative to AAm) MBA as a crosslinker and 2.8 wt% (relative to AAm) APS as an initiator were added into the solution. Finally, 0.2% (relative to solution) TEMED as catalyst was added. The obtained solution was transferred into a petri-dish to form the PAM/agar/CNT self-healing conductive hydrogel. The method to the fabricated battery was the same as the above mentioned.

Measurements for the changes in water weight of electrode and electrical conductivity. Changes in the water weight and electrical conductivity of the electrode were measured at the same time. The hydrogel electrode was placed on a hot plate with a temperature of 80 ℃ to be fully dehydrated. Subsequently, the fully dehydrated hydrogel electrode was attached to the hydrogel electrolyte to be rehydrated to equilibrium. During the whole process, the weight and resistance of the sample were recorded. The m/m_0 represented the ratio of the real-time water weight in the electrode to the water weight in the pristine hydrogel electrode during the dehydration and rehydration process. The conventional calculation method of water content is $M_{water}/M_{water} + M_0$, where M_{water} is the real time water weight in the electrode, and M_0 is the weight of the dehydrated electrode. Since the water content in the electrode was changed

in real-time, the denominator in the formula was also changed. This resulted in no comparative significance in the electrode water content at different periods. m/m_0 was performed at the same time as the standard, which could accurately represent the real-time change of water in the electrode. The electrical conductivity (σ, $mS \cdot cm^{-1}$) of the electrode was calculated by the equation of $\sigma = \frac{L}{1000R \cdot W \cdot d}$, where L (cm) is the length of the hydrogel electrode, R (Ω) is the resistance of the electrode, W (cm) is the width of the electrode, and d (cm) is the thickness of the electrode.

Different rehydration ratios of hydrogel electrodes. First, changing the water contents of hydrogel electrolytes to 70%, 80%, 89%, and 95% (LiCl was not involved in the calculation of water content). The ratios of the monomer, crosslinker, and initiator remained the same. And the concentration of the LiCl also remained the same. Then, the dehydrated electrodes with different rehydration ratios were obtained by attaching to the same size electrolytes with different water contents.

Mechanical characterization. To measure Young's moduli, the hydrogel electrodes, hydrogel electrolytes and all-hydrogel batteries were prepared in the rectangular shape (10 mm × 40 mm). A fixed rate of stretching (50 $mm \cdot min^{-1}$) was applied to all tensile tests. The Young's moduli were calculated from the slopes of the linear segment of the stress-strain curves.

The adhesive energy was measured through a bilayer structure. For the stacked interface, the pristine hydrogel electrode was directly attached to the electrolyte. For the fused interface, the dehydrated electrode was attached to the electrolyte and absorbed water for equilibrium. The sizes of the electrode and electrolyte were both 10 mm × 40 mm, and the backs were both bonded to a polyethylene terephthalate (PET) film with Krazy glue. The free ends of the electrode and electrolyte were on the same side. During the peeling experiment, the free ends of bilayer-structured samples and the PET stiff backings were attached to the machine grips. All tests were conducted with a constant peeling speed of 50 $mm \cdot min^{-1}$. Adhesive energy was calculated by dividing two times the plateau force by the width of the bilayer-structured samples. The adhesive energy between the hydrogel and wet tissue was measured with the same method by attaching hydrogel to pork.

The shear strength was measured similar to the adhesive energy. The difference was that the electrode and electrolyte were attached face to face, and the free ends of the electrode and electrolyte were on the opposite side.

Heartbeat detection system. All animal experiments were reviewed and approved by the Animal Experimentation Committee of Nanjing University of Chinese Medicine with the approval/accreditation number 202106A004. The conductive hydrogel was used as a hydrogel

strain sensor. The fully charged all-hydrogel battery was employed as a power source. Hydrogel strain sensor, fully charged hydrogel battery and detector (CorrTest CS350) were assembled in series in the circuit. After the New Zealand rabbit was placed under anesthesia, the chest was opened to expose the heart. The biofluids on the heart were removed using gauze. The detection system was attached to the heart without any glue. The heartbeat was mimicked by introducing cyclical, pressurized air inputs into the heart chambers. When the strain sensor deformed with the heart, the internal resistance of the sensor changed, and the current fluctuation detected by the detector was the heartbeat signal.

Detecting for the permeation of Li^+ ions. Detection for the permeation of Li^+ ions. The all-hydrogel lithium-ion batteries were immersed in 100 mL deionized water. 10 mL solution was taken to conduct the inductively coupled plasma (ICP) test after 1, 3, 7, and 15 days (n = 3). The obtained Li^+ concentration was used to calculate the Li^+ content in 100 mL immersion solution and compared with 100 mL deionized water.

***In vitro* biocompatibility.** The cell culture was carried out using the all-hydrogel battery-conditioned media. 10 mg all-hydrogel lithium-ion battery was incubated in 1 mL Dulbecco's modified eagle medium (DMEM) for 24 hours. The DMEM without incubating all-hydrogel battery was used as a control. 100 μL of mouse fibroblasts (L929), mouse skeletal muscle cells (C2C12) and human umbilical vein endothelial cells (HUVEC) (iCell Bioscience Inc, Shanghai) were incubated in a 96-well plate (1×10^4 cells per well) (n = 3 per each group) at 37 ℃ in a 5% CO_2 humidified atmosphere. Then the cell was incubated with the all-hydrogel battery-conditioned media for 24 hours at 37 ℃ in a 5% CO_2 humidified atmosphere. The cells were treated with a 10 μL Cell Counting Kit-8 (Beyotime Biotechnology) for 1 hour at 37 ℃ in a 5% CO_2 humidified atmosphere. The optical absorptance value (450 nm) was measured using the UV-vis spectrophotometer (TECAN, infinite M200 PRO). For fluorescent images, the cells were rinsed with 1 × PBS thrice, then stained by 250 μL Calcein/PI Cell Viability/Cytotoxicity Assay Kit (Beyotime Biotechnology) for 30 min at 37 ℃, and observed by fluorescence microscope (Axio Vert A1).

In *vivo* biocompatibility. All animal experiments were reviewed and approved by the Animal Experimentation Committee of Nanjing University of Chinese Medicine with the approval/accreditation number 202108A014. The female ICR mice (20-25 g) were used for the implantable experiments. The all-hydrogel lithium-ion batteries were prepared in an aseptic manner and disinfected under ultraviolet light for 30 min. The size of the all-hydrogel batteries was 0.3 × 0.3 × 0.1 cm. The mice were first anesthetized with 3% isoflurane. Then removed the back hair of the mice and placed the animals on a heating pad. 1 cm skin incision was made in the center of the mouse's back. To create space for implant placement, performed a blunt dissection from the incision to one side. The samples were placed in subcutaneous bags (n = 5). The controls were not implanted after the incision of the skin (n =

5). The incisions were closed with interrupted sutures. After implantation 15 and 30 days, blood samples were acquired from the orbital venous plexus for hematology and blood chemistry tests. After the mice were euthanized, the major organs (heart, liver, spleen, lung and kidney) were excised and fixed with paraformaldehyde (4% v/v) for histological analysis by hematoxylin and Eosin (H&E) staining.

Characterization. The structure was characterized through X-ray diffraction (XRD, Shimadzu LabX XRD-6100). The morphologies were characterized by scanning electron microscopy (SEM, HITACI S4800). All-hydrogel batteries were first frozen with liquid nitrogen and then freeze-dried by a vacuum freeze dryer (SCIENTZ-10N) to completely drain the water. For the fluorescence microscope, Rhodamine B was firstly added to the hydrogel electrolyte. Then, the hydrogel electrolyte was used to fabricate an all-hydrogel battery. Finally, the interface was characterized by a fluorescence microscope (Axio Vert A1). The mechanical properties were characterized using a mechanical testing machine (50N load-cell, HY-0580). Infrared thermal images were captured by an infrared camera (Fotric 225-1).

Electrochemical performance tests. For a three-electrode system, the cyclic voltammetry and galvanostatic charge-discharge were carried out by an electrochemical working station (CorrTest CS350) with 2 M LiCl aqueous electrolyte in argon. Ag/AgCl electrode and excessive activated carbon were used as reference and counter electrodes, respectively. The electrochemical performance of all-hydrogel batteries was tested by the electrochemical working station (CorrTest CS350) and the multichannel electrochemical testing system (LAND CT2001). Electrochemical impedance analysis and alternating current impedance spectra were obtained from an electrochemical working station (CorrTest CS350). For the test on the skin, we had obtained informed written consent from a volunteer. The all-hydrogel battery adhered to the wrist of the volunteer. The discharge curve was measured when the wrist was repeatedly bent and released.

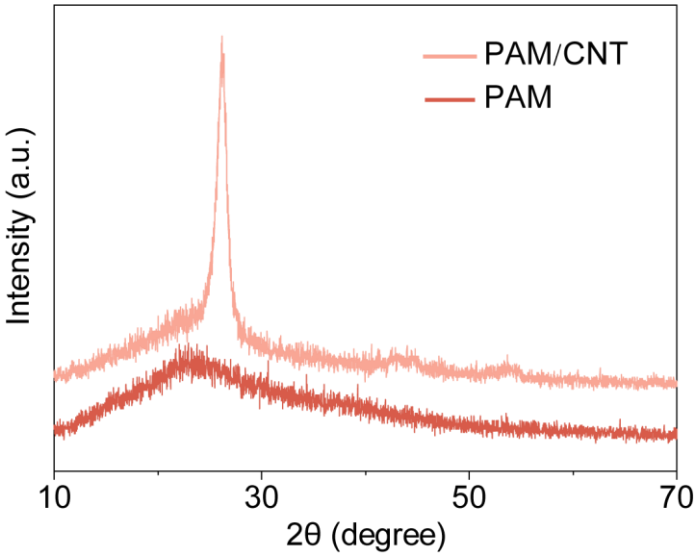

Figure S1. XRD patterns of PAM and PAM/CNT hydrogel.

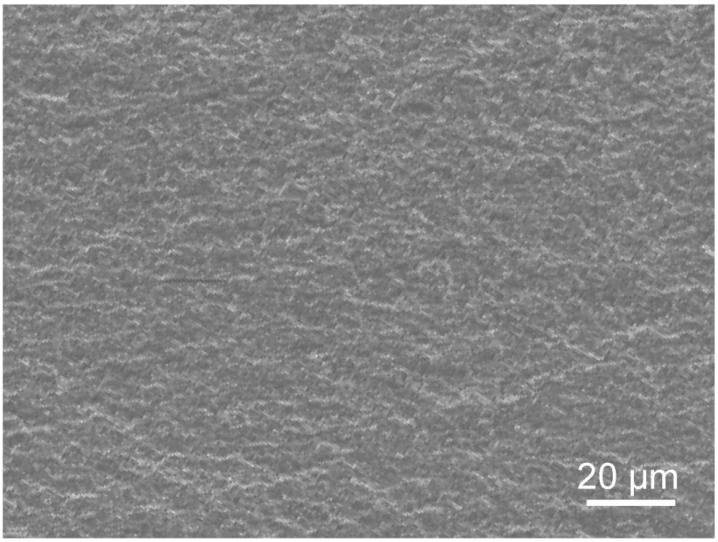

Figure S2. SEM image of the dehydrated PAM/CNT electrode.

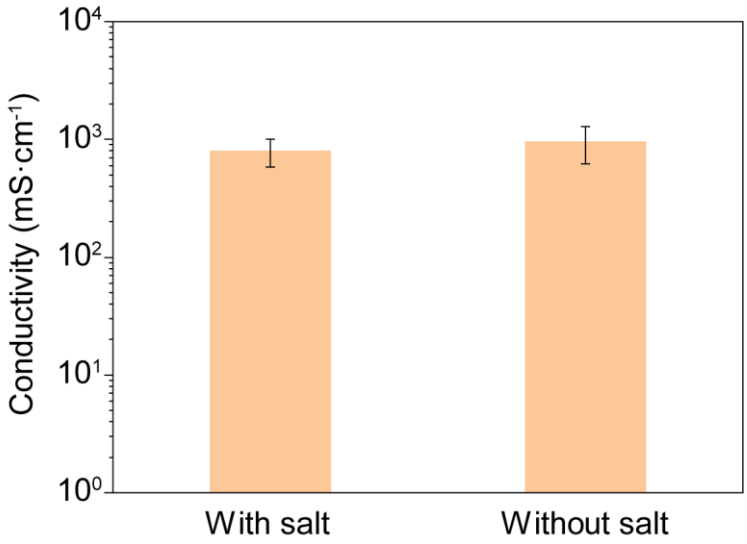

Figure S3. Electrical conductivities of rehydrated electrodes attached to electrolyte with and without LiCl electrolyte salt, respectively (n = 3).

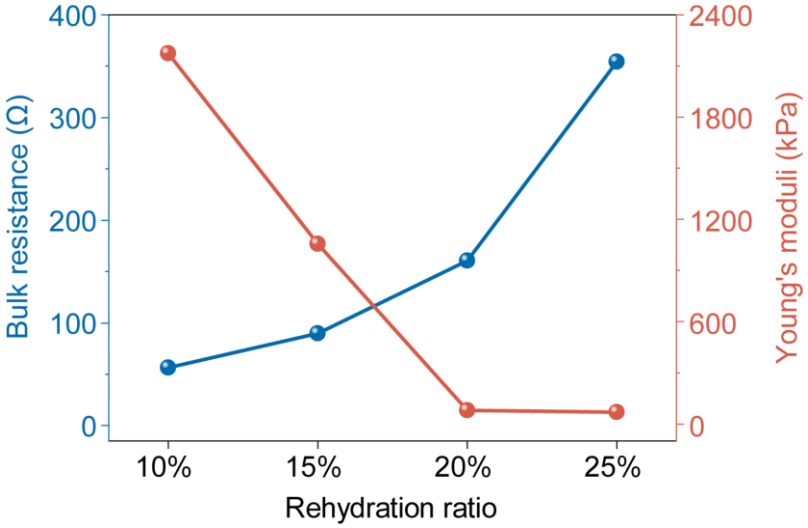

Figure S4. Bulk resistance and Young's moduli of all-hydrogel batteries based on different rehydration ratios of rehydrated hydrogel electrodes.

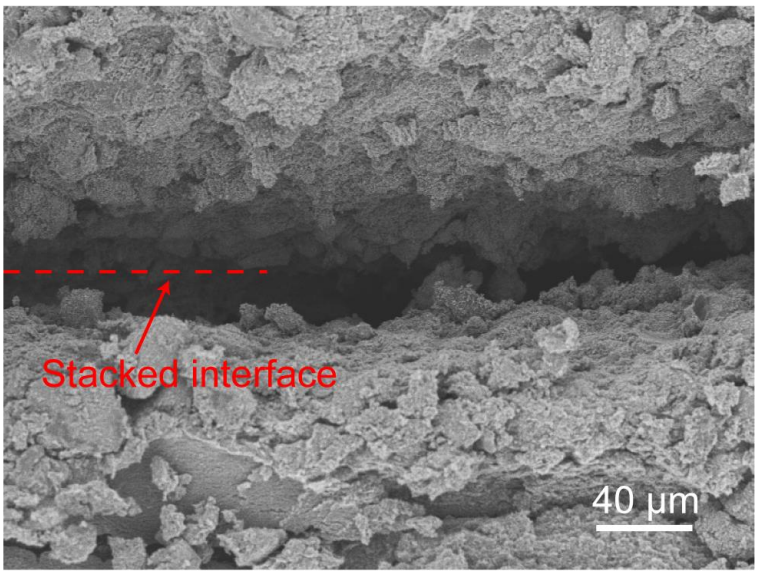

Figure S5. SEM image of the interface between pristine hydrogel electrode and electrolyte.

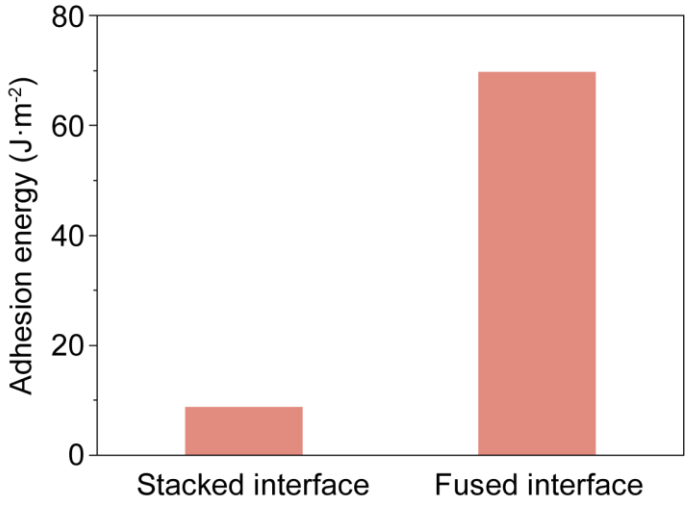

Figure S6. Adhesion energy between hydrogel electrode and electrolyte for fused and stacked interfaces.

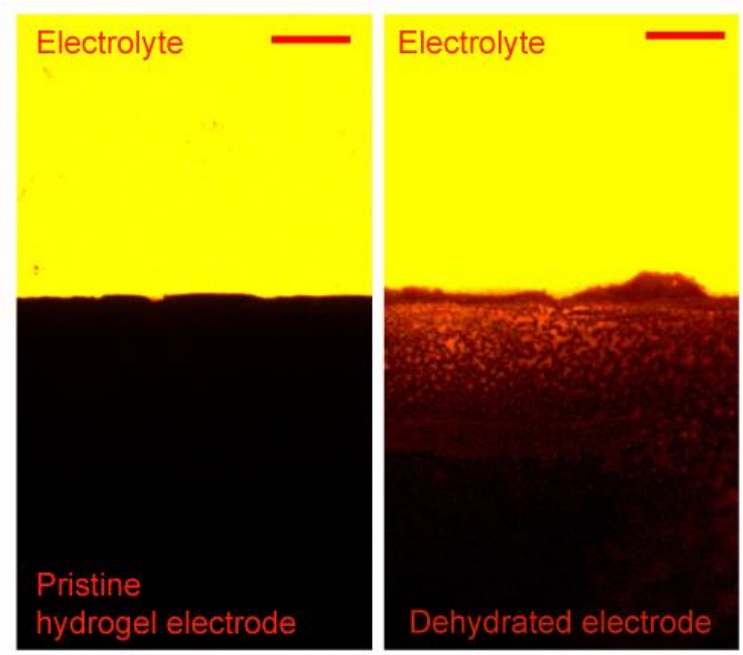

Figure S7. Fluorescence microscope for the diffusion of water in two electrodes (scale bar: 200 μm). The yellow part was the electrolyte with a fluorescent agent, and the black part was the electrode. The two electrodes were attached to the electrolytes for the same time. No fluorescent substance was observed in the pristine hydrogel electrode, indicating that the water on the surface or interior of the electrolyte did not diffuse into the electrode. The region where the dehydrated electrode was in contact with the electrolyte exhibited obvious fluorescence, indicating that the water on the surface and interior of the electrolyte slowly diffused into the electrode.

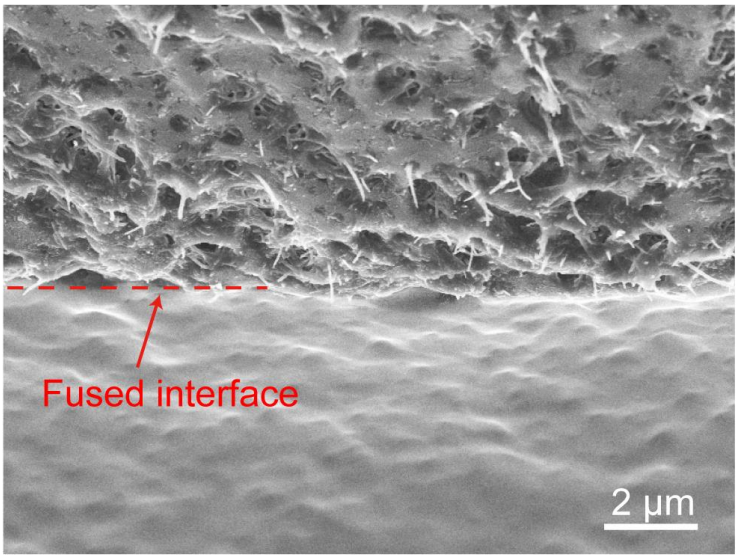

Figure S8. SEM image of the interface between rehydrated hydrogel electrode and electrolyte.

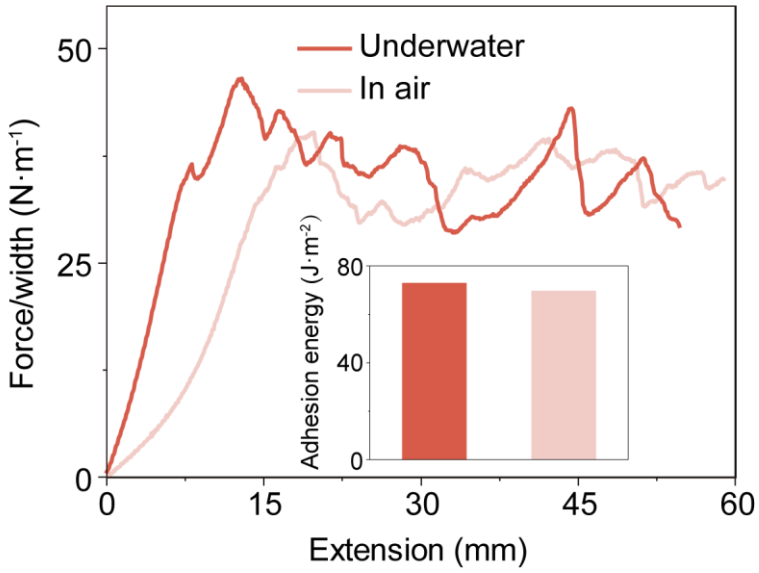

Figure S9. The interface adhesion curves of the all-hydrogel batteries in different environments. Insert: corresponding interface adhesion energy. The all-hydrogel battery was immersed in water for 24 hours to explore the influence of the wet environment on interface adhesion.

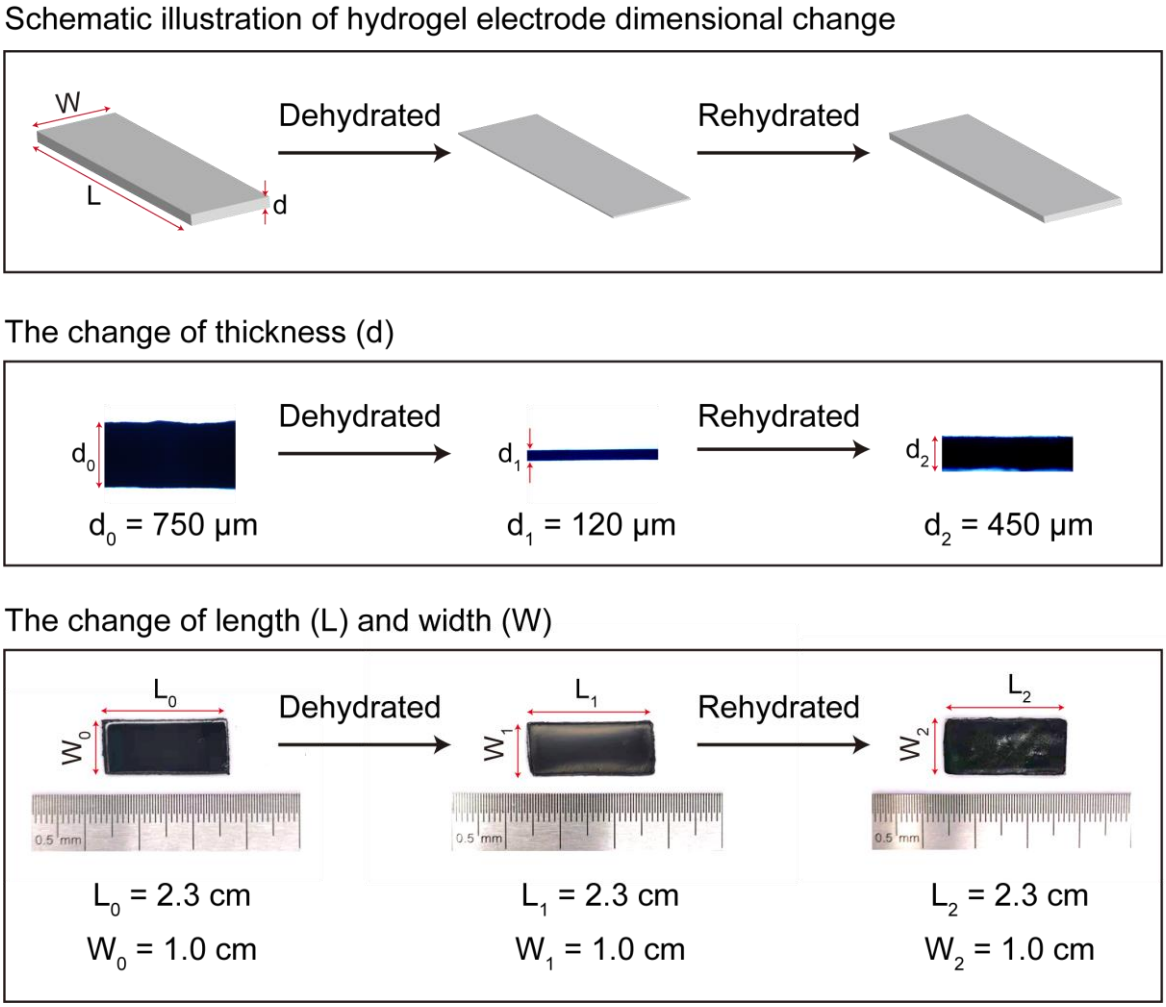

Figure S10. Schematic illustration and photographs of pristine hydrogel electrode (left), dehydrated electrode (middle) and rehydrated hydrogel electrode (right). The thickness was decreased and then increased during dehydration and rehydration, respectively. Both length and width remained unchanged during dehydration and rehydration.

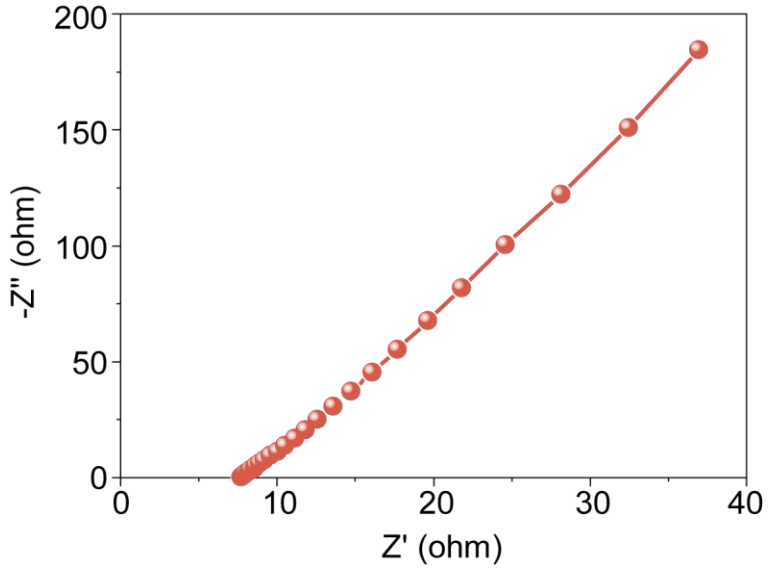

Figure S11. Alternating current impedance spectra of PAM/LiCl hydrogel electrolyte at a frequency range from 1 Hz to 100 kHz.

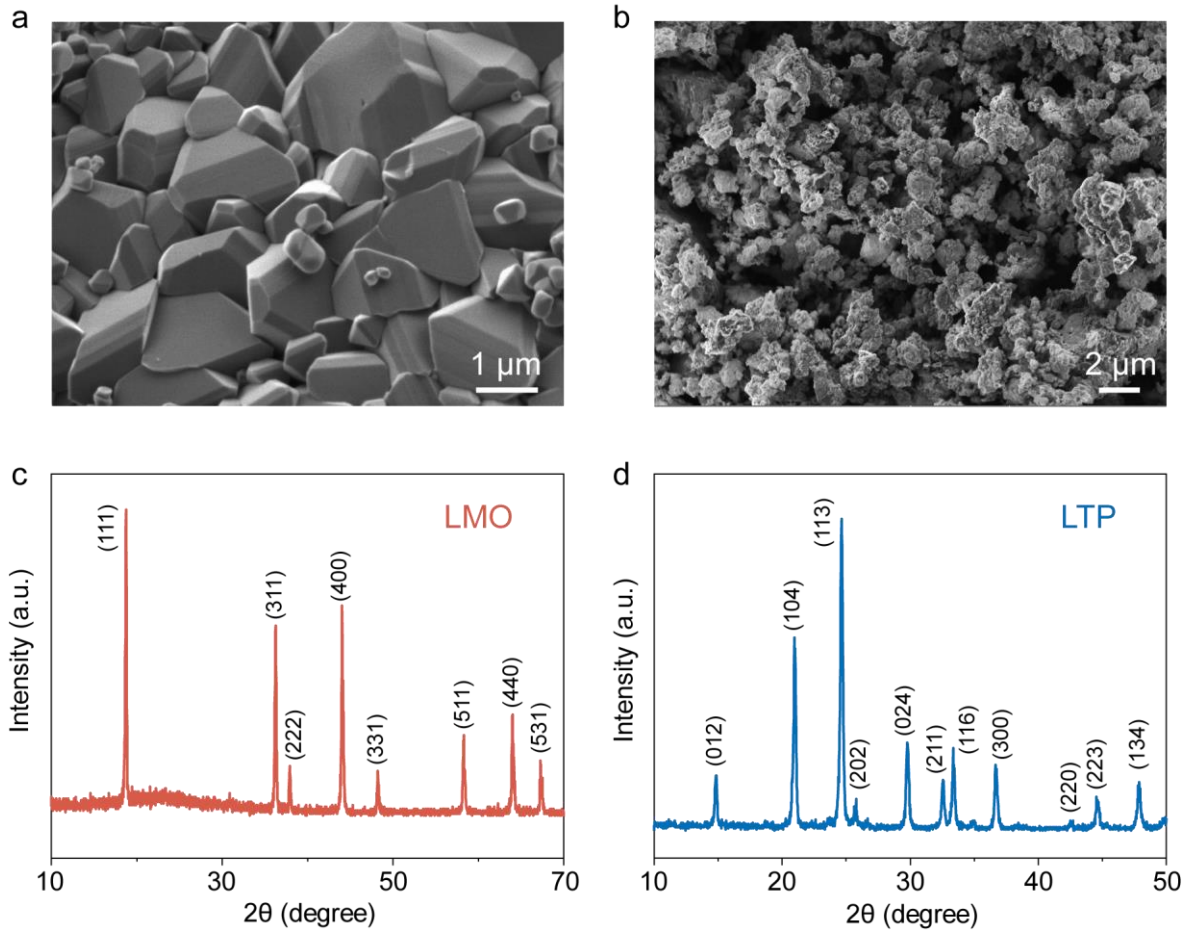

Figure S12. SEM images of (a) LMO and (b) LTP and XRD patterns of (c) LMO and (d) LTP. LMO was spinel phase and LTP was NASICON-type phase.

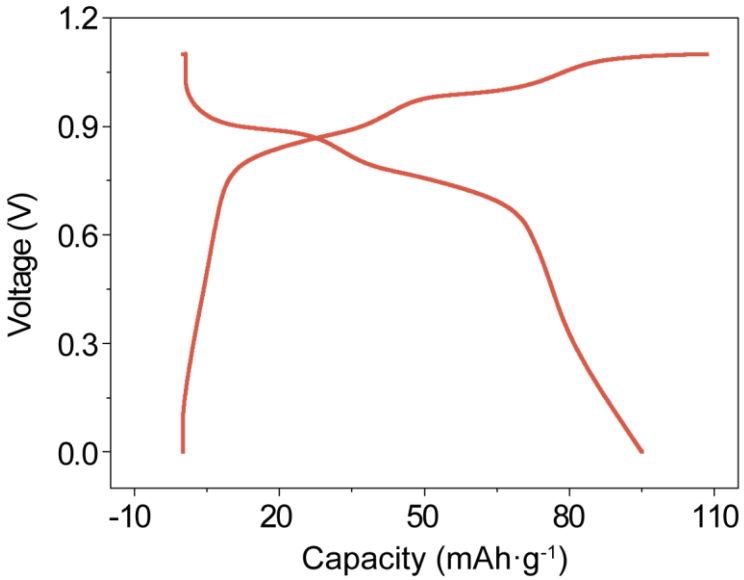

Figure S13. Galvanostatic charge-discharge curves of rehydrated PAM/CNT-LMO hydrogel electrode at a current density of 0.5 $A \cdot g^{-1}$.

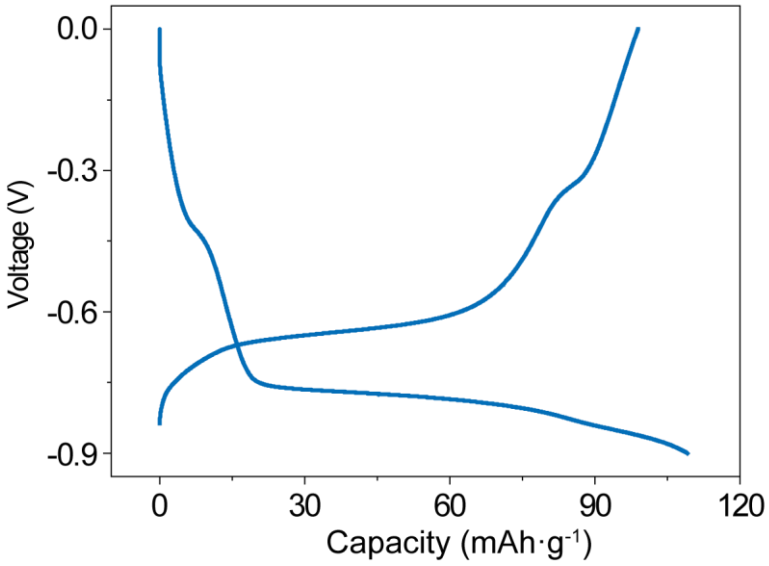

Figure S14. Galvanostatic charge-discharge curves of rehydrated PAM/CNT-LTP hydrogel electrode at a current density of 0.5 $A \cdot g^{-1}$.

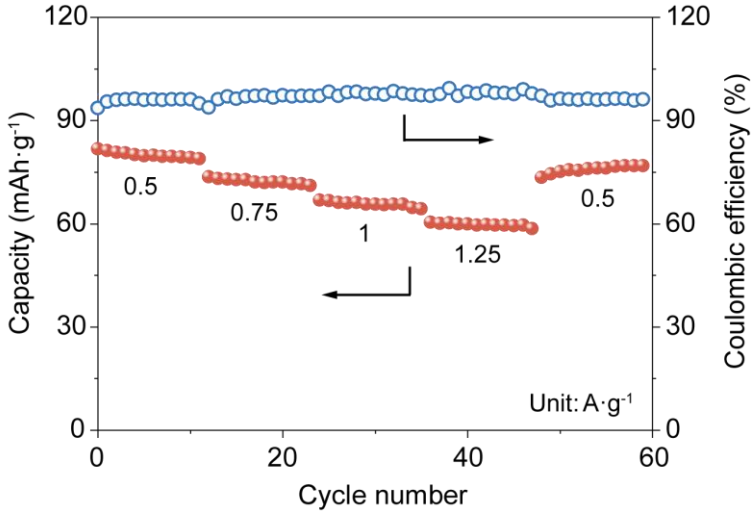

Figure S15. The rate capability of all-hydrogel lithium-ion battery.

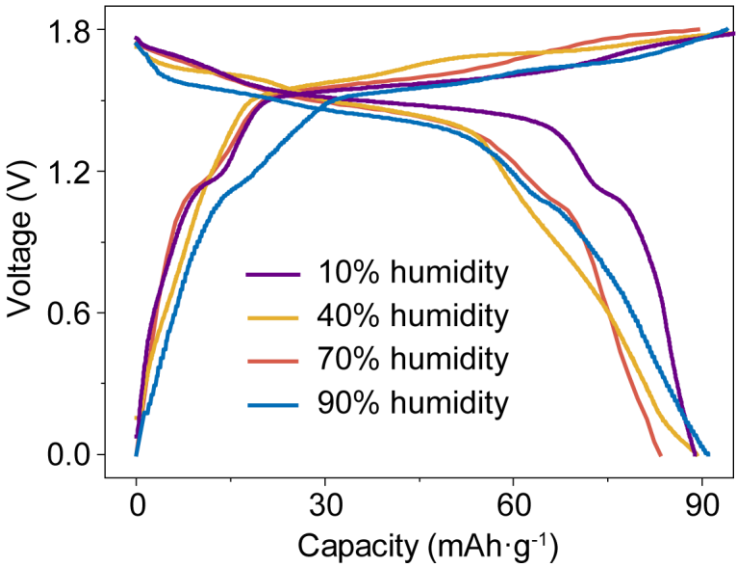

Figure S16. Galvanostatic charge-discharge curves of the all-hydrogel batteries at a current density of 0.5 $A \cdot g^{-1}$ in environments with different humidity. The 70% humidity corresponded to the test environment of the battery in Figure 3. The humidity was adjusted by the desiccant and water vapor.

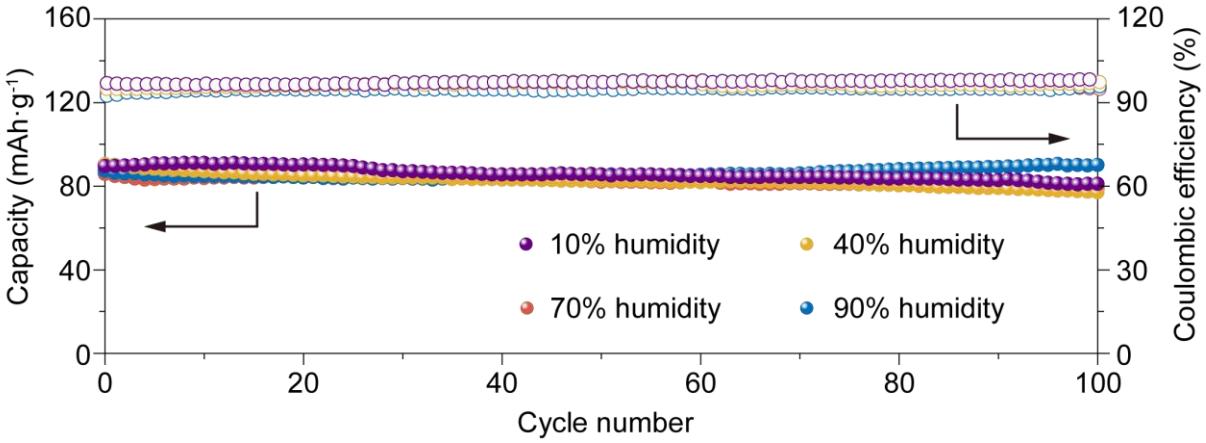

Figure S17. Cyclic performance of all-hydrogel battery at a current density of 0.5 $A \cdot g^{-1}$ in the environments with different humidity.

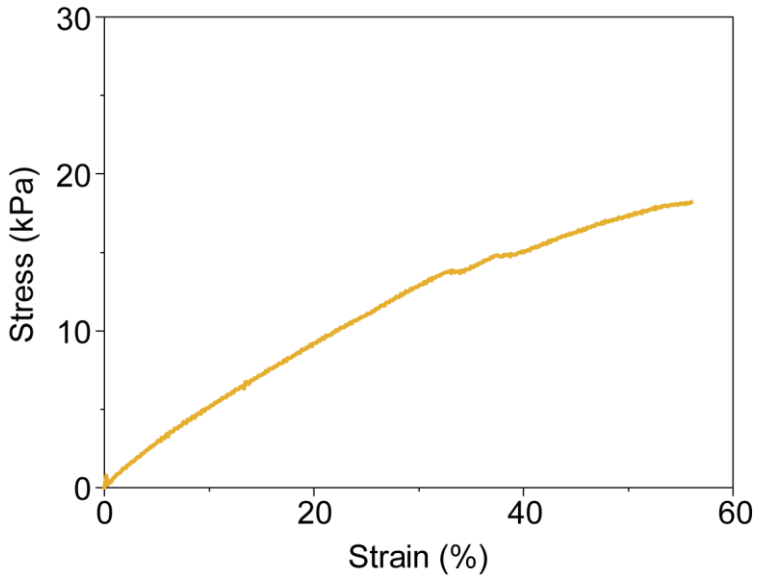

Figure S18. Stress-strain curves of encapsulation layer for the all-hydrogel battery.

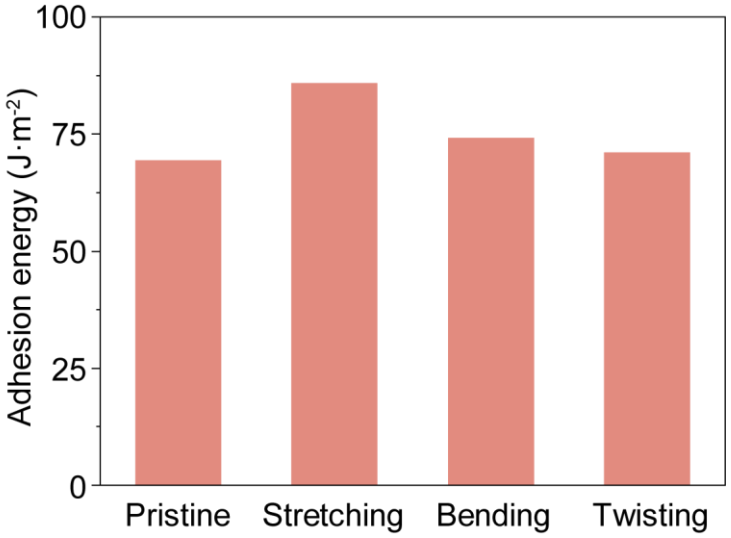

Figure S19. Adhesion energy of the battery interface before and after different deformations with each for 1,000 cycles.

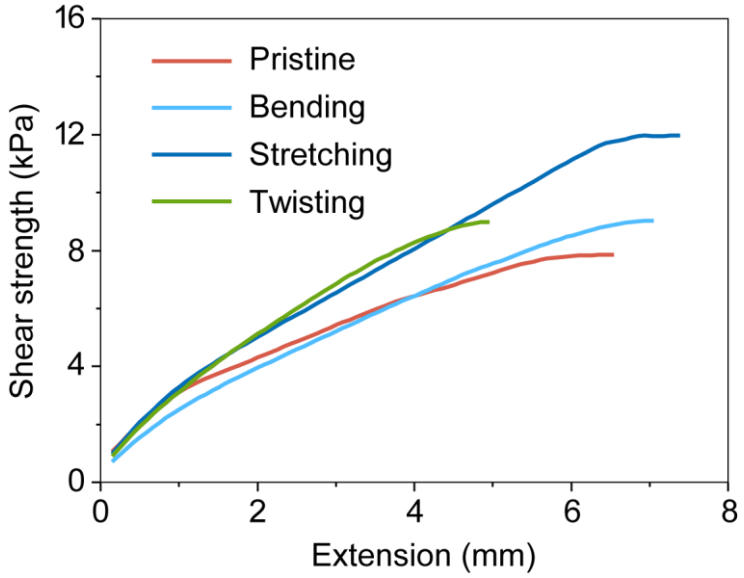

Figure S20. Shear strength of the all-hydrogel battery interface before and after different deformations with each for 1,000 cycles.

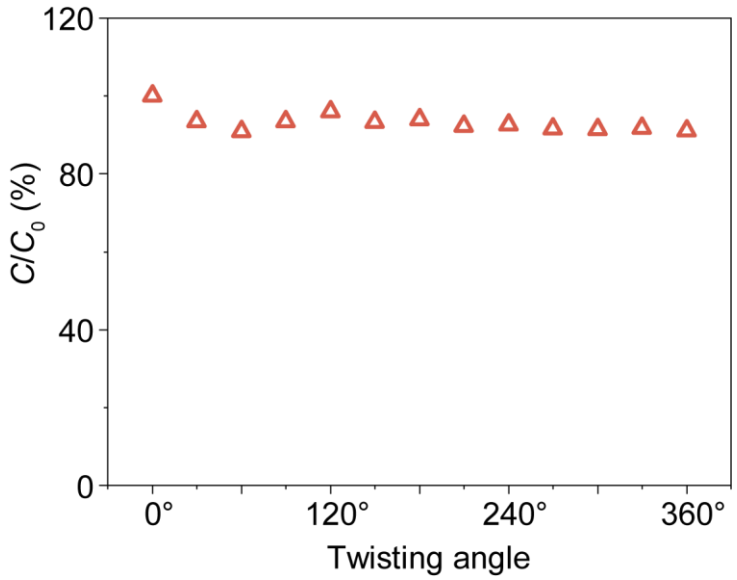

Figure S21. Specific capacitance retention of all-hydrogel battery at different twisting angles. C_0 and C correspond to specific capacities before and after twisting, respectively.

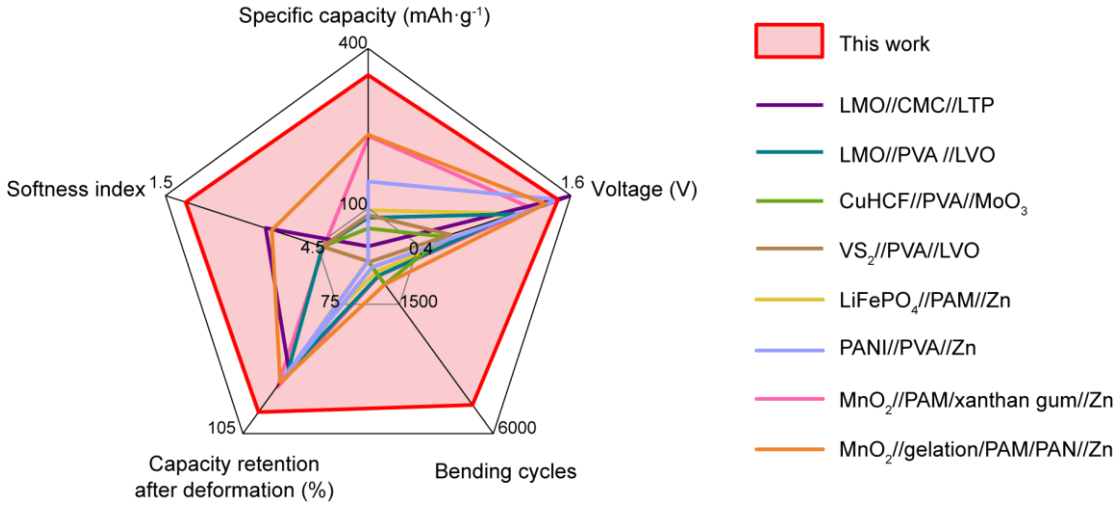

Figure S22. The comparison of electrochemical performance and flexibility of the all-hydrogel batteries and the reported flexible batteries based on the hydrogel. Softness index = lg (Young's moduli, kPa). The data were provided in Table S1.

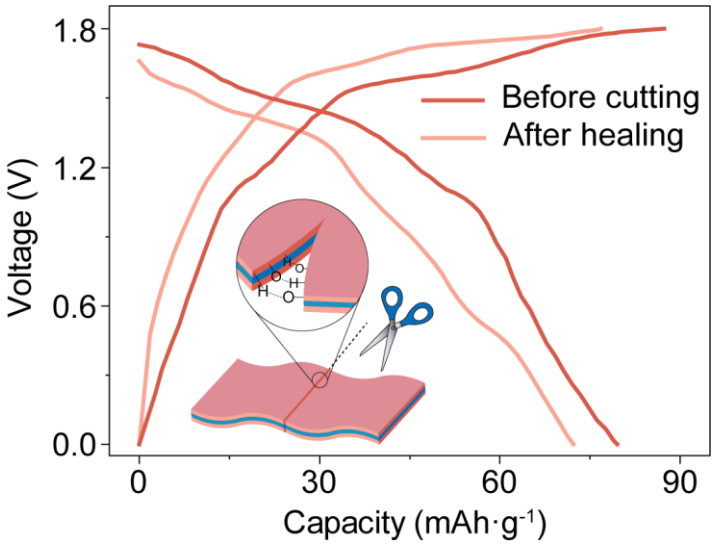

Figure S23. Galvanostatic charge-discharge curves of all-hydrogel self-healing battery with PAM/agar/CNT electrode before cutting and after healing at a current density of 0.5 $A \cdot g^{-1}$.

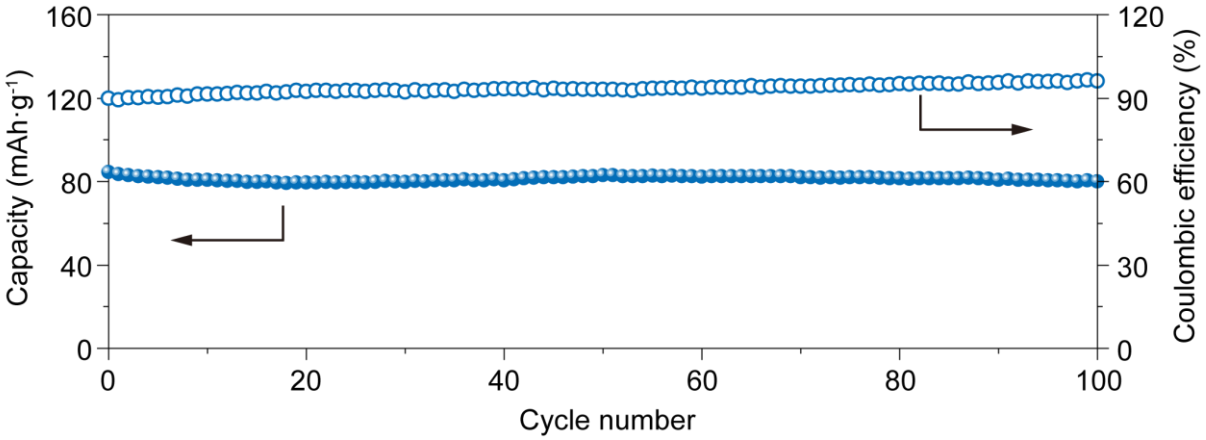

Figure S24. Cyclic performance of the all-hydrogel battery at 36 ℃ (the temperature of the wrist) at a current density of 0.5 $A \cdot g^{-1}$. The battery was first put into a ziplock bag and then immersed in 36 ℃ water bath for the electrochemical test.

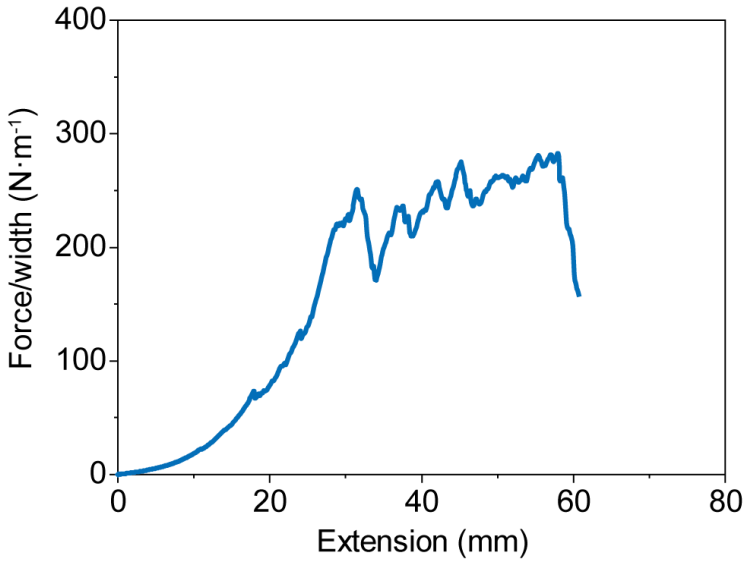

Figure S25. The adhesion curve between the polyacrylic acid-chitosan-tannic acid-Al^{3+} hydrogel and wet tissue. The adhesion energy was 488 J m^{-2}.

Figure S26. Photograph of the interface between all-hydrogel battery and heart.

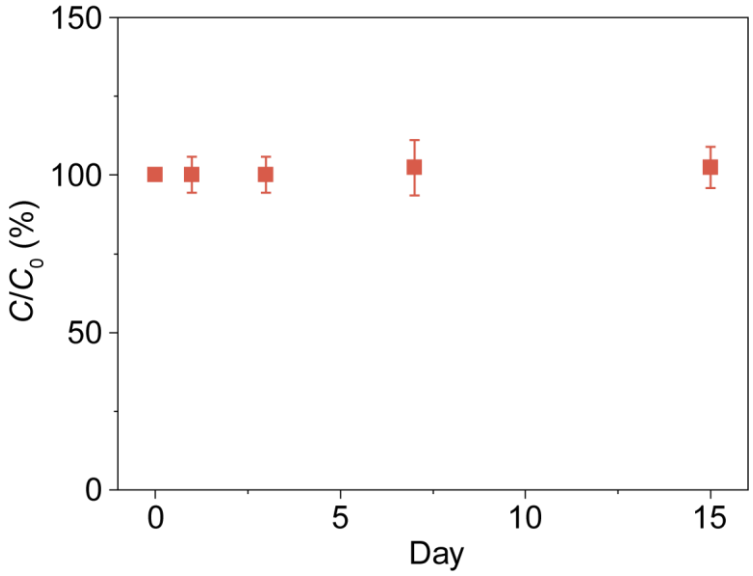

Figure S27. The change of Li^+ content in the aqueous solution when the all-hydrogel lithium-ion battery was immersed in deionized water for 0–15 days (n = 3). The 0 day represents deionized water without immersing the battery. Here C_0 and C correspond to the Li^+ content at 0 and other days, respectively.

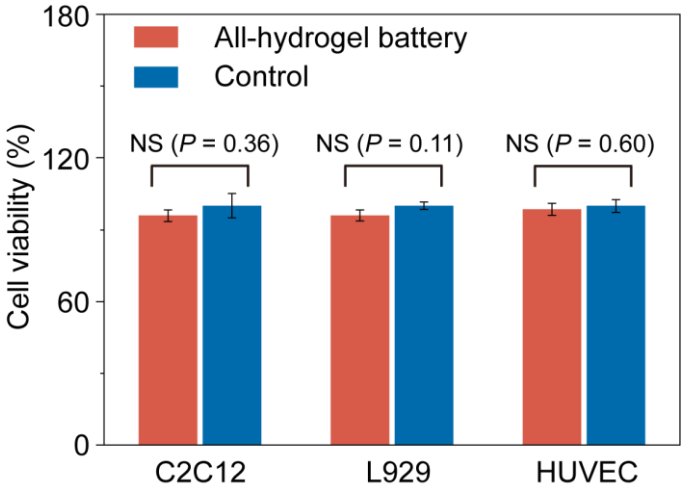

Figure S28. *In vitro* cell viability of C2C12, L929 and HUVEC after 24 hours culture with the all-hydrogel battery-conditioned cell culture media and controls (n = 3).

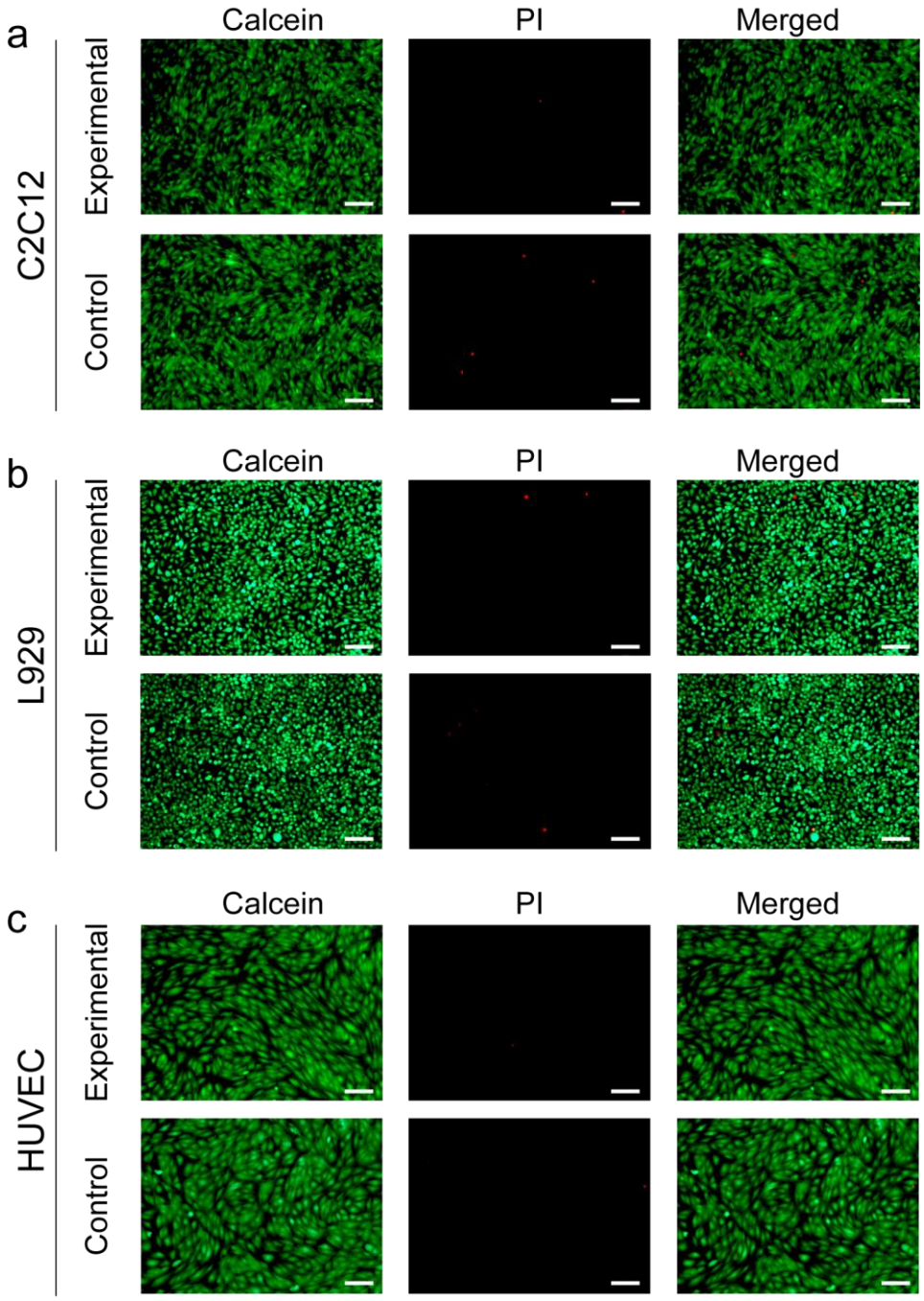

Figure S29. Fluorescent images of (a) C2C12, (b) L929 and (c) HUVEC after 24 hours of culture with the all-hydrogel battery-conditioned cell culture media and controls stained by LIVE/DEAD viability/cytotoxicity assay kit (scale bar: 100 μm, n = 3).

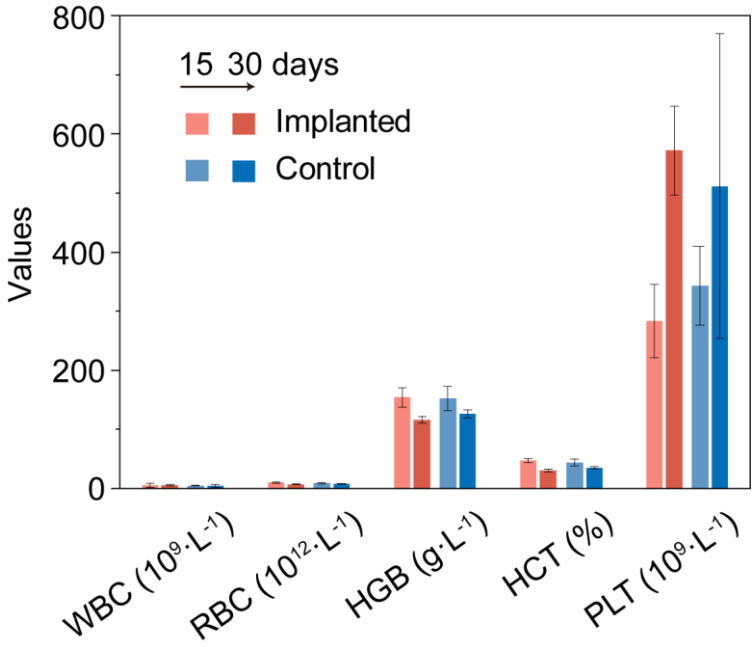

Figure S30. The average counts of white blood cell (WBC), red blood cell (RBC), hemoglobin (HGB), platelet (PLT) and hematocrit (HCT) after implantation for 15 and 30 days (n = 5).

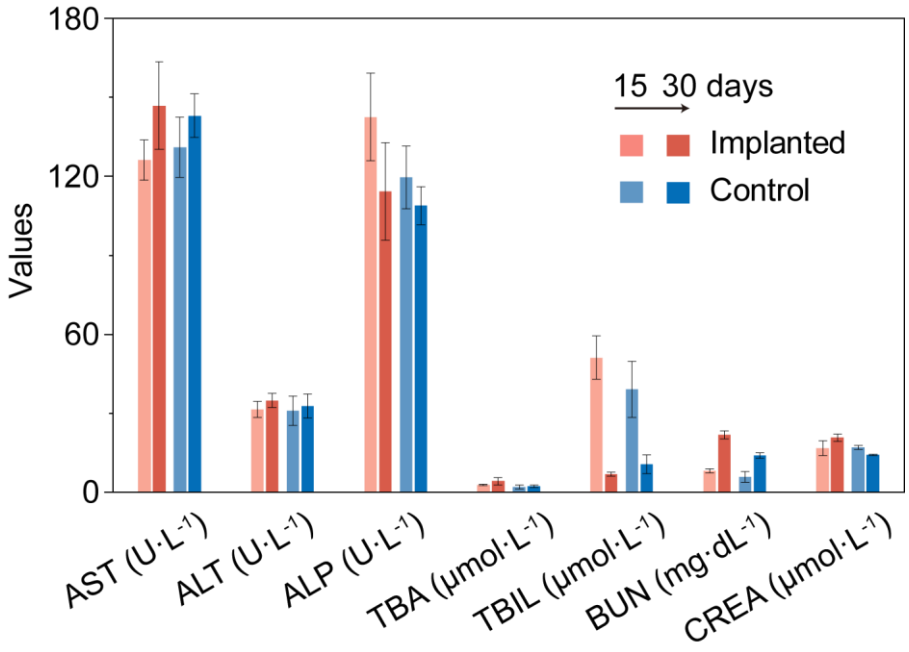

Figure S31. The blood levels of aspartate transaminase (AST), alaninetransaminase (ALT), alkaline phosphatase (ALP), total bile acid (TBA), total bilirubin (TBIL), blood urea nitrogen (BUN) and creatinine (CREA) after implantation for 15 and 30 days (n = 5).

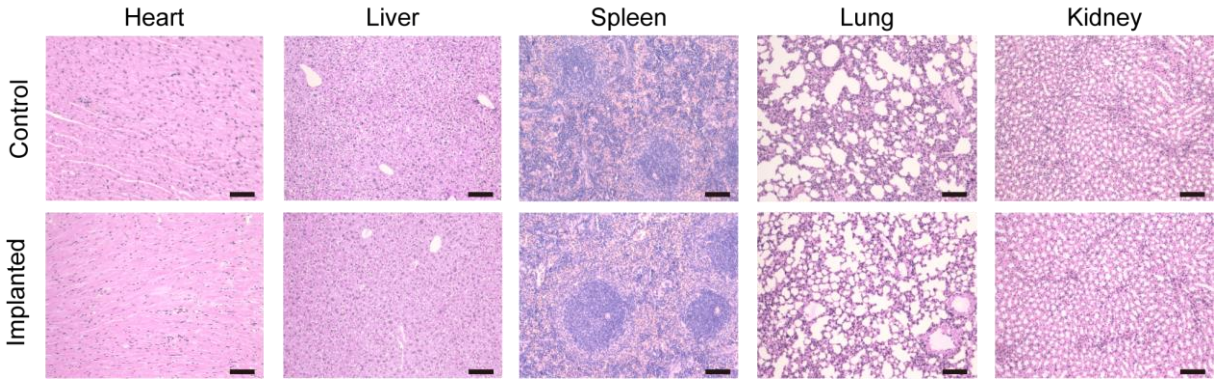

Figure S32. The histological data (representative H&E stained sections) of the major organs, including heart, liver, spleen, lung and kidney of control and implanted group for 15 days (scale bar: 100 μm, n = 5).

Table S1. The comparison of electrochemical performance and flexibility of the all-hydrogel battery and the reported flexible batteries based on the hydrogel.

Flexible batteries	Specific capacity ($mAh \cdot g^{-1}$)	Deformation	Cycles	Capacity retention (%)	Ref.
All-hydrogel batteries	370 at 0.5 $A \cdot g^{-1}$	Bending 180°, stretching 30%, twisting 90°	5000	100	This work
CNT/LMO/CNT //CMC-Li_2SO_4// CNT/LTP/CNT	28.2 at 0.5 $A \cdot g^{-1}$	Bending 60°	200	90.3	[1]
Carbon cloth-LMO //PVA-$LiNO_3$// Carbon cloth-LVO	81.92 at 0.5 $A \cdot g^{-1}$	Bending 60°	500	90.7	[2]
Carbon cloth-CuHCF //PVA-$Al(NO_3)_3$// Carbon cloth-MoO_3	62 at 0.5 $A \cdot g^{-1}$	Bending	800	55	[3]
Carbon cloth-VS_2 //PVA-$Zn(CH_3COO)_2$-$Mn(CH_3COO)_2$// Carbon cloth-Zn	87 at 0.5 $A \cdot g^{-1}$	Bending 180°	30	65	[4]
Carbon cloth-$LiFePO_4$ //PAM-$ZnSO_4$-LiCL//Zn foil	95 at 0.44 $A \cdot g^{-1}$	Bending 180°	400	80	[5]
CNT felt-PANI//PVA-$Zn(CF_3SO_3)_2$//Zn foil	150 at 0.5 $A \cdot g^{-1}$	Bending 180°	200	91.7	[6]
Carbon cloth-CNT paste-MnO_2 //PAM-xanthan gum-$ZnSO_4$-$MnSO_4$// carbon cloth-Zn	237 at 0.308 $A \cdot g^{-1}$	Bending 180°	500	94.5	[7]
CNT paper-MnO_2 //gelation/PAM/PAN $ZnSO_4$-$MnSO_4$// CNT paper-Zn	238 at 0.6 $A \cdot g^{-1}$	Bending 180°	800	93.1	[8]

Refence:

[1] Y. Zhao, Y. Zhang, H. Sun, X. Dong, J. Cao, L. Wang, Y. Xu, J. Ren, Y. Hwang, I. Son, X. Huang, Y. Wang, H. Peng, *Angew. Chem., Int. Ed.* **2016**, *55*, 14384-14388.

[2] Liu Z, Li H, Zhu M, et al. Z. Liu, H. Li, M. Zhu, Y. Huang, Z. Tang, Z. Pei, Z. Wang, Z. Shi, J. Liu, Y. Huang, C. Zhi, *Nano Energy* **2018**, *44*, 164-173.

[3] P. Wang, Z. Chen, Z. Ji, Y. Feng, J. Wang, J. Liu, M. Hu, H. Wang, W. Gan, Y. Huang, *Chem. Eng. J.* **2019**, *373*, 580-586.

[4] J. Liu, J. Long, Z. Shen, X. Jin, T. Han, T. Si, H. Zhang, *Adv. Sci*. **2021**, *8*, 2004689.

[5] M. Zhu, X. Wang, H. Tang, J. Wang, Q. Hao, L. Liu, Y. Li, K. Zhang, O. G. Schmidt, *Adv. Energy. Mater.* **2019**, *30*, 1907218.

[6] F. Wan, L. Zhang, X. Wang, S. Bi, Z. Niu, J. Chen, *Adv. Funct. Mater.* **2018**, *28*, 1804975.

[7] B. Wang, J. Li, C. Hou, Q. Zhang, Y. Li, H. Wang, *ACS Appl. Mater. Interfaces* **2020**, *12*, 46005-46014.

[8] H. Li, C. Han, Y. Huang, Y. Huang, M. Zhu, Z. Pei, Q. Xue, Z. Wang, Z. Liu, Z. Tang, Y. Wang, F. Kang, B. Li, C. Zhi, *Energy Environ. Sci.* **2018**, *11*, 941-851.